Journal of Climate

Hydroclimatic Controls on the Means and Variability of Vegetation Phenology and Carbon Uptake

--Manuscript Draft--

Manuscript Number:	
Full Title:	Hydroclimatic Controls on the Means and Variability of Vegetation Phenology and Carbon Uptake
Article Type:	Article
Corresponding Author:	Randal Koster, Sc.D. NASA/GSFC Greenbelt, MD UNITED STATES
Corresponding Author's Institution:	NASA/GSFC
First Author:	Randal Koster, Sc.D.
Order of Authors:	Randal Koster, Sc.D.
	Gregory K. Walker
	George J. Collatz
	Peter E. Thornton
Abstract:	Long-term, global offline (land-only) simulations with a dynamic vegetation phenology model are used to examine the control of hydroclimate over vegetation-related quantities. First, with a control simulation, the model is shown to capture successfully (though with some bias) key observed relationships between hydroclimate and the spatial and temporal variations of phenological expression. In subsequent simulations, the model shows that: (i) the global spatial variation of seasonal phenological maxima is controlled mostly by hydroclimate, irrespective of distributions in vegetation type, (ii) the occurrence of high interannual moisture-related phenological variability in grassland areas is determined by hydroclimate rather than by the specific properties of grassland, and (iii) hydroclimatic means and variability have a corresponding impact on the spatial and temporal distributions of gross primary productivity (GPP).
Suggested Reviewers:	Sietse Los s.o.los@swan.ac.uk Expert on vegetation/climate interactions
	Zong-Liang Yang liang@jsg.utexas.edu Climate/hydrology expert
	Michael Puma michael.j.puma@nasa.gov Climate/vegetation expert
	Josh Fisher Joshua.B.Fisher@jpl.nasa.gov Water and carbon cycle expert
	Guiling Wang gwang@engr.uconn.edu Climate/vegetation expert

Cost Estimation and Agreement Worksheet

Click here to download Cost Estimation and Agreement Worksheet: Cost Estimation and Agreement Worksheet.pdf

Hydroclimatic Controls on the Means and Variability of Vegetation Phenology and Carbon Uptake

R. D. Koster[1], G. K. Walker[1,2], G. J. Collatz[3], and P. E. Thornton[4]

[1]Global Modeling and Assimilation Office, NASA/GSFC, Greenbelt, MD

[2]SSAI, Lanham, MD

[3]Biospheric Sciences Laboratory, NASA/GSFC, Greenbelt, MD

[4]Environmental Sciences Division, Oak Ridge National Laboratory, Oak Ridge, TN

August 8, 2013

Corresponding author address:

Randal Koster

Global Modeling and Assimilation Office

Code 610.1, NASA/GSFC

Greenbelt, MD 20771

randal.d.koster@nasa.gov

Abstract

Long-term, global offline (land-only) simulations with a dynamic vegetation phenology model are used to examine the control of hydroclimate over vegetation-related quantities. First, with a control simulation, the model is shown to capture successfully (though with some bias) key observed relationships between hydroclimate and the spatial and temporal variations of phenological expression. In subsequent simulations, the model shows that: (i) the global spatial variation of seasonal phenological maxima is controlled mostly by hydroclimate, irrespective of distributions in vegetation type, (ii) the occurrence of high interannual moisture-related phenological variability in grassland areas is determined by hydroclimate rather than by the specific properties of grassland, and (iii) hydroclimatic means and variability have a corresponding impact on the spatial and temporal distributions of gross primary productivity (GPP).

1. Introduction

Recognition that the Earth's energy and water cycles are intrinsically entwined is longstanding (e.g., Budyko 1971). The land surface energy and water balances both feature evapotranspiration as a dominant term, and the generation of rainfall (a key component of the water cycle) has a profound effect on the heat budget of the atmosphere. The inseparability of the energy and water cycles underlies their joint treatment in numerous analyses (e.g., Trenberth et al. 2011) and the formation of international research projects addressing their linkage, such as GEWEX (the Global Energy and Water Exchanges Project, part of the World Climate Research Programme, or WCRP).

The Earth's carbon cycle is in turn intrinsically entwined with the energy and water cycles. Vegetation health (and associated carbon uptake) is affected by water availability; deserts, for example, tend not to be carbon sinks. Conversely, carbon affects the water and energy cycles; the transpiration of water from vegetation and the associated cooling of the land surface are in large part controlled by the efficiency of the vegetation's uptake of carbon dioxide (e.g., Berry et al. 2010), and the build-up of vegetation through carbon uptake has a direct impact on land surface albedo – how much of the sun's radiation is absorbed by the surface. Carbon dioxide is, of course, also a greenhouse gas. The basic connection between the surface fluxes of water, energy, and carbon is appropriately recognized in numerous studies (e.g., Leuning et al. 2004; Bowling et al. 2010), and it is a motivation for such international research projects as ILEAPS (the Integrated Land Ecosystem Atmosphere Study, another component of WRCP).

In this paper, we focus in particular on the carbon-water linkage at the land surface. A number of relevant studies in the literature have shared this focus. Using data collected at a number of flux tower sites in North America, Knapp and Smith (2001) provided a powerful,

64 geographically diverse analysis of the connections between the surface water and carbon cycles –
65 specifically, of the controls of precipitation means and variability on aboveground net primary
66 production (ANPP). Their results show that carbon uptake by the land surface is indeed strongly
67 regulated by precipitation characteristics, with maximum uptake related strongly to precipitation
68 amount and with the interannual variability of the uptake maximized in grassland areas, where
69 both precipitation variability and vegetation cover are adequately high. Remotely sensed
70 measurements of vegetation properties allow for an even more comprehensive and large-scale
71 analysis of connections between carbon and climatic variables, including precipitation (e.g.,
72 Fang et al. 2005, Iichi et al. 2010, Jahan and Gan 2011). In a recent global analysis, Zeng et al.
73 (2013) uncovered strong relationships between the interannual variations contained in a
74 multidecadal NDVI dataset (normalized difference vegetation index, an indicator of green leaf
75 area) and antecedent precipitation levels, particularly in temperate and tropical grasslands.

76 A modeling framework is a natural venue for studying the connections between carbon
77 and water. Wang and Eltahir (2000), using a simple coupled biosphere-atmosphere model,
78 showed how the interaction between vegetation and precipitation can lead to multiple equilibria
79 for vegetation state. Zeng et al. (1999) showed, again with a simple coupled model, how
80 vegetation-climate interactions may affect the nature of precipitation variability in the Sahel.
81 Puma et al. (2013) used a modeling framework to compare the impacts of meteorological
82 variability and phenological variability on the simulation of surface moisture and carbon fluxes.
83 Complex and relatively complete models of vegetation behavior, models that indeed tie together
84 explicitly the interactions between carbon, energy, and water fluxes at the land surface and
85 accordingly allow the prediction of vegetation state, are arguably the new state-of-the-art in
86 numerical climate modeling. Sellers et al. (1997) pointed to the explicit treatment of carbon as a

logical step in the evolution of land surface treatments in Earth system models; dynamic vegetation models (DVMs) following this evolutionary path are already being used at major climate modeling centers (e.g., Lawrence et al. 2010, Krinner et al. 2005, Boussetta et al. 2012, Dunne et al. 2013).

An advantage of using a modeling framework for carbon-water studies is the potential for doing unique analyses that isolate and illustrate the mechanisms that control the transfers of water and carbon across the land surface. Carefully formulated modifications of a physical process treatment or of a variable that forces it can be imposed, and the resulting impacts on surface fluxes can be quantified and analyzed, thereby elucidating the role of the process examined. A second important advantage of such models is their ability to provide data fields that are unattainable with in situ measurement networks or even satellite-based sensors. Gross primary productivity (GPP), for example, can only be measured directly at a limited number of flux tower sites. A DVM, however, if driven with observations-based meteorological forcing, can potentially produce estimates of GPP at high spatial and temporal resolution across the globe. Such estimates would be biased relative to nature, of course, due to deficiencies in model formulation and forcing data; still, if care is given to their interpretation, the estimates do have scientific value.

Both of these advantages come into play in the present paper, in which we use the dynamic phenology component of an established DVM together with the water and energy balance framework of a hydrology-focused LSM to characterize, on a global scale, the controls of precipitation means and variability on GPP – both on its spatial distribution and on its temporal variability across the globe. The modeling system used (described in Section 2) is indeed found to be effective in capturing the key hydroclimatic controls on phenology that

operate in nature (as demonstrated in Section 3). The simulated GPP distributions from the thus-validated system are analyzed jointly with global precipitation data in Section 4. The model experiments provide new insights into the relative impacts of precipitation means, precipitation variability, and vegetation type in determining GPP distributions.

2. Dynamic Phenology Model

The dynamic phenology model used in this study is in essence a merger of the carbon physics of the NCAR/DOE CLM4 dynamic vegetation model (Oleson et al. 2010) with the energy and water balance formulations of the NASA Global Modeling and Assimilation Office (GMAO) Catchment land surface model (LSM) (Koster et al. 2000). We provide here a brief description of these two components and the technique used to merge them into a new model, hereafter referred to as the Catchment-CN LSM (i.e., the Catchment LSM with carbon and nitrogen physics).

The NCAR/DOE Community Land Model, version 4 (CLM4), represents prognostic coupled energy, water, carbon, and nitrogen cycles in a framework that permits global-scale as well as regional and site-level simulation. The global-scale parameterization used here includes specification of sub-grid heterogeneity in plant functional type (PFT) distributions, with multiple PFTs assigned fractional area coverage within each grid cell, where they compete with one another for available soil moisture and mineral nitrogen resources. In this prescribed biogeography mode the fractional areas occupied by individual PFTs do not change, but vegetation growth, soil heterotrophic activity, carbon stocks, and other ecosystem states (such as leaf area index) do vary prognostically (Thornton et al. 2009).

The GMAO Catchment land surface model is a state-of-the-art surface energy and water budget model designed for use with global Earth system models. As with most other LSMs, the Catchment LSM employs complex treatments of land surface flux generation, tying the efficiency of evaporation and runoff generation to the moisture and temperature states of the land surface, and it includes parameterizations of vegetation impacts on transpiration, canopy interception, albedo, and surface roughness. Relatively unique to the Catchment LSM is its treatment of the subgrid variability of soil moisture and temperature, which is explicitly tied to a description of the topographic variability in the region modeled – in the Catchment LSM, valley bottoms within a given grid element are explicitly modeled as being wetter, and the hilltops are explicitly modeled as being drier. Runoff and evaporation are calculated independently in the different hydrological regimes, using regime-specific physics.

In essence, in merging the two models, we retain the Catchment LSM's energy and water balance calculation framework while using the NCAR/DOE CLM4 carbon balance calculations. The approach is illustrated in Figure 1. In the original Catchment LSM (Figure 1a), the model uses forcing from the atmosphere along with prescribed vegetation phenology (LAI and greenness fraction) and the current values of LSM temperature and moisture prognostic variables to compute the canopy conductance, the parameter describing the ease with which the plants transpire water. The canopy conductance, computed separately for each hydrological regime, is then used in each regime's energy balance and water balance calculations, which in turn provide the fluxes of heat and moisture to the atmosphere.

Figure 1b shows the approach used by the merged system, the Catchment-CN LSM. The atmospheric inputs are now fed first into the components of the NCAR/DOE model that update the carbon states and compute, as a matter of course, canopy conductances that reflect an explicit

155 treatment of photosynthesis physics. These canopy conductances, along with the leaf area
156 indices diagnosed from the new carbon prognostic variables, are fed into the energy and water
157 balance calculations of the original Catchment LSM. The output fluxes with the merged system
158 include a net carbon flux.

159 The merger of the two models allows the Catchment-CN LSM to follow 19 distinct
160 vegetation types, a significant increase from the six independent types followed with the original
161 Catchment LSM. Furthermore, the unique character of the original Catchment LSM allows for
162 the independent monitoring of carbon variables in the different topographically-defined
163 hydrological regimes. Figure 2 describes our methodology. Each land surface element is
164 subdivided into three static carbon zones defined by topography, through analysis of the
165 distribution of the compound topographic index (Moore et al., 1993). The first zone, covering a
166 fixed 10% of the area, represents the valley bottoms; this zone tends to be generally wet. The
167 second and third zones represent the lower (drier) hillslopes and upper (even drier) hillslopes,
168 respectively. Through areal weighting, soil moisture and temperature information from the
169 dynamically-varying hydrological zones are combined for use by the carbon physics in the fixed
170 vegetation zones, as indicated in the figure. Separate sets of carbon prognostic variables are
171 followed in each vegetation zone, and thus each zone generates a different manifestation of
172 phenology. When examining the model results, we find that green vegetation indeed tends to be
173 densest in the valley bottoms.

174 Some additional modifications to the NCAR/DOE vegetation model were needed to
175 optimize its performance in the GMAO system. To prevent some occasional singular behavior –
176 namely, the catastrophic shutdown of vegetation during cold spells and a resulting overgrowth of
177 the vegetation during the subsequent year – we replaced a particular set of vegetation types (crop

178 and temperate shrubs/grass) that feature a strong response to temperature stress by a mix of two
179 different types: one that is seasonally deciduous and one that is not. Neither of the replacement
180 types employ the temperature stress shutdown, though both respond to moisture stress; the
181 proportion of the mix applied is defined by latitude, and the replacement is indeed limited to the
182 latitude band 32°-42° in both hemispheres. Outside of this latitudinal band, we limit the number
183 of coexisting PFTs in each static carbon zone to two. Also, we modified the NCAR/DOE
184 vegetation physics to allow half of the new carbon assimilated by deciduous types to be
185 displayed during the current year rather than in the following year, which brings certain
186 measures of our interannually-varying phenology more in line with observations. Finally,
187 whereas the NCAR/DOE vegetation model uses the previous year's annual mean temperature to
188 determine certain onset triggers, we use a climatological mean temperature.

189 In our main ("control") application of the model, the prescribed distributions of
190 vegetation type follow those used by the default 0.5°×0.5° version of CLM4 (Oleson et al. 2010).
191 Vegetation phenology and carbon states, however, evolve freely. The model is run globally
192 offline (i.e., disconnected from an atmospheric model) on high-resolution catchments (roughly
193 20-30 km in size) over the period 1948-2008, using the observations-based meteorological
194 forcing of Sheffield et al. (2006); the simulation loops over this period more than 30 times to
195 ensure spin-up and equilibration of the carbon storage reservoirs. The output data examined
196 (phenological variables, carbon fluxes, etc.) are aggregated to 2°×2.5° for processing.

197

198 **3. Evaluation Against Observations**

199 To test the realism of the model's connections between hydroclimate and vegetation
200 variables, we focus on two distinct aspects of global phenological expression: the global spatial

pattern of long-term phenological means and the interannual variability of phenology at a given location. These are discussed in turn following a brief description of the observations.

a. Observations used

We examine satellite-based products of NDVI (normalized difference vegetation index) and FPAR (fraction of absorbed photosynthetically active radiation), both of which increase with green vegetation cover. The NDVI data is a subset of the latest version of the Global Inventory and Mapping Studies, or GIMMS, data (Tucker et al. 2005). The data's native resolution is semiweekly at 8 km, and the data span the period July 1981-present. For our analyses we aggregate these data to a 2.5°×2.5° degree, monthly resolution for the period 1982-2010. The data are derived from the Advanced Very High Resolution Radiometer (AVHRR) instrument with known limitations compared to the more advanced MODIS instrument (Kaufman et al. 1998). However, the longer temporal coverage of GIMMS relative to MODIS (29 versus 11 years) and the good correspondence between their measurements (Tucker et al. 2005, Beck et al. 2011) makes it well suited to the analysis presented here.

The FPAR data are derived directly from the NDVI data using the method of Los et al. (2000). The method combines the NDVI-based FPAR estimation technique of Sellers et al. (1996) with that of Choudhury (1987) and Goward and Huemmrich (1992); the combination provides estimates that are well behaved relative to available in-situ observations. The relationship between NDVI and FPAR underlying this combined approach is monotonic but nonlinear. Note that it is also somewhat vegetation dependent, so that the conversion of global

NDVI data to global FPAR data requires a global field of vegetation types. Thirteen years of FPAR data are available, spanning the period 1997-2009.

As will be seen below, the sensitivities of the NDVI and FPAR data to hydroclimatic variation are similar in many ways. Both are worth illustrating here. The NDVI values are constructed directly from spectral reflectance measurements and thus represent a raw form of the observations. While the construction of the FPAR values requires some additional assumptions regarding vegetation behavior, FPAR has the distinct advantage of representing a physically meaningful phenological variable, one that can be compared directly to output from the Catchment-CN model.

The global precipitation data used here consist of monthly precipitation totals for 1979-present at 2.5°×2.5° degree resolution, as produced by the Global Precipitation Climatology Project as part of their Version 2 Satellite-Gauge dataset (Adler et al. 2003; see also ftp://precip.gsfc.nasa.gov/pub/gpcp-v2.2/doc/V2.2_doc). Satellite-based data contributing to the product, in varying capacities and over various periods and regions, include Special Sensor Microwave/Imager (SSM/I) passive microwave estimates, Television-Infrared Observation Satellite (TIROS) Operational Vertical Sounder (TOVS) estimates, and the Adjusted Geostationary Operational Environmental Satellite (GOES) Precipitation Index (Adler et al. 1994). A wealth of surface rain gauges is used to adjust the multi-sensor precipitation estimates over land. Hall et al. (2006) provide background on the accuracy of the GPCP product; of note is the higher uncertainty of the product over mountains, deserts, high latitudes, and undeveloped areas due in large part to a lower density of rain gauges.

245 b. Impact of hydrological variations on the mean spatial distributions of phenological variables

246 To deal with the fact that NDVI shows significant seasonal variability, with different
247 regions having different peak months for the index, we examine a quantity we will call $NDVI_{max}$.
248 We compute, at each 2.5°×2.5° grid cell, the average seasonal cycle of NDVI from the GIMMS
249 data and then identify the month for which the average NDVI is highest. $NDVI_{max}$ is set to the
250 average value for the 3-month period centered on this peak month. (Note that under this
251 definition, the values for $NDVI_{max}$ in adjacent grid cells may be taken from different 3-month
252 periods.) Figure 3a shows the global distribution of $NDVI_{max}$ as derived from the spatially
253 aggregated GIMMS data. The distribution mirrors known vegetation distributions, with large
254 values in tropical, deciduous, and boreal forests, intermediate values in grassland and shrubland
255 areas, and small values in the deserts.

256 Figure 4a shows how the spatial distribution of $NDVI_{max}$ in Figure 3a correlates with
257 various meteorological quantities. The first four bars of each panel show the square of the
258 spatial correlation (r^2, across land surface grid cells) of $NDVI_{max}$ with, respectively, annual mean
259 precipitation, the standard deviation of annual precipitation, annual mean air temperature, and
260 annual mean net radiation. (The base-10 logarithms of the precipitation quantities are in fact
261 used here. Temperature and net radiation information are derived from the full period of the
262 Sheffield et al. (2006) dataset. The outgoing longwave component of the net radiation is
263 estimated using the surface air temperature in that dataset.) The salient result from the figure is
264 the dominance of the two precipitation quantities in determining the spatial structure of NDVI.
265 Multiple regression of $NDVI_{max}$ on the mean and variability of precipitation produces an r^2 of
266 about 0.55 (fifth bar), and adding the temperature and net radiation information to the multiple

regression does not significantly increase the r^2 (sixth bar). These results underlie the importance of hydroclimate in determining the spatial distribution of phenological maxima.

Figure 5a shows more directly how $NDVI_{max}$ is related to precipitation means and variability. Each dot in Figure 5a corresponds to a 2.5°×2.5° land grid cell. The size and color of the dot is determined by the local value of $NDVI_{max}$, as indicated by the legend. The dot's abscissa is determined by the mean annual precipitation at that grid cell, and the dot's ordinate refers to the interannual variability of precipitation there. (Note the logarithmic scales.) The precipitation and NDVI quantities are computed over consistent time periods; for example, if a grid cell's peak NDVI, as computed from the GIMMS data for 1982-2010, occurs in July, then precipitation means and variances are computed from nineteen September-August yearly totals starting with the total for the period September 1981-August 1982.

Two features of the scatter plot stand out. The first reflects an expected result: a minimum average precipitation must be achieved to attain moderately high $NDVI_{max}$ levels. The plot shows this minimum value to be roughly 1 mm/day; the dots to the left of this threshold (which include, of course, all desert points) show low values of $NDVI_{max}$. The second, and more intriguing, feature of the scatter plot is the tendency for $NDVI_{max}$ to decrease as the standard deviation of precipitation increases. This feature is illustrated more clearly in Figure 5b, which shows a binned version of the scatter plot data; to generate this plot, an array of boxes is overlain on Figure 5a, and the $NDVI_{max}$ values for the points within each box are averaged. For a given value of the mean precipitation, especially for values above 1 mm/day, $NDVI_{max}$ clearly tends to decrease with increasing σ_P. This presumably reflects the reduced ability of vegetation to flourish when the year-to-year supply of water is less stable.

289 We also examine in this context the analogous variable $FPAR_{max}$, the average value of a
290 grid cell's FPAR for the 3-month period centered on the peak FPAR month, as determined from
291 the local climatological cycle. Figure 3b shows the distribution of $FPAR_{max}$ as computed from
292 the GIMMS data. As might be expected, given that FPAR in GIMMS is derived from NDVI, the
293 spatial distributions in Figures 3a and 3b are very similar, as are the spatial correlations with the
294 meteorological forcing variables (Figure 4b). Figures 5c and 5d show the precipitation-based
295 scatter plots for the $FPAR_{max}$ values. Average water supply (mean precipitation) and water
296 supply stability (σ_P) are seen to impose dual control over $FPAR_{max}$ as well; the sensitivity of
297 FPAR to hydroclimate is indeed very similar to that of NDVI.

298 How well does the Catchment-CN model perform? The model produces diagnostics for
299 both the incident and absorbed photosynthetically active radiation; we take the ratio of these
300 quantities to produce the model's FPAR values. Figure 3c shows the global distribution of
301 simulated FPAR in the peak 3-month period; note that for a given location, this peak period may
302 differ from that for the observations. Two features of the simulated FPAR distribution stand out.
303 First, the simulated spatial patterns agree well with the observed patterns in Figure 3b. Second,
304 there are, nonetheless, apparent biases in the simulated FPAR values, with the highest simulated
305 values being too large and the lowest being too small. Such biases presumably reflect
306 deficiencies in the model, though they may also stem partially from limitations in the forcing
307 data or in the observational FPAR values themselves. The biases must be kept in mind
308 throughout our analysis.

309 The square of the spatial correlation of simulated FPAR with meteorological forcing
310 variables (Figure 4c) agrees quite well with the corresponding values found for observed FPAR
311 (Figure 4b). The simulated r^2 values with the temperature and net radiation variables are slightly

312 higher, but these values are still quite low. Figure 4 shows that, in strong agreement with the
313 observations, variations in hydroclimate explain most of the FPAR variability seen in the model.

314 The agreement in spatial pattern with a presence of bias also manifests itself in the
315 precipitation-based scatter plot in Figure 5e and the corresponding binned version of the plot in
316 Figure 5f. In agreement with the observations, the model clearly shows an increase in FPAR
317 with increasing precipitation and with decreasing precipitation variability. Overall, the model,
318 though biased, does appear to simulate realistic controls of hydroclimatic variation over
319 phenological means.

320

321 c. Impact of hydrological variations on the interannual variability of phenological variables

322 As a second and somewhat independent test of the ability of the Catchment-CN model to
323 capture observed links between carbon and water variables, we examine the interannual
324 variability of vegetation phenology. Rather than examining the total variance of a variable such
325 as summertime NDVI, we focus instead on a modified quantity, one that captures the carbon-
326 water connection:

327 $$\mathrm{Var(NDVI)^*} = \mathrm{Var(NDVI)}\ \mathrm{Corr^2(NDVI,P)}\ , \qquad (1)$$

328 where Var(NDVI) is the interannual variance of 3-month NDVI averages (again centered on the
329 peak NDVI month, based on the climatological seasonal cycle), $\mathrm{Corr^2(NDVI,P)}$ is the correlation
330 between these individual NDVI averages and the corresponding yearly precipitation totals (with
331 the end of the precipitation averaging period corresponding to the end of the 3-month NDVI
332 averaging period), and Var(NDVI)* is interpreted as the portion of the NDVI variance associated
333 with variations in moisture availability. That is, we are employing here the standard

334 interpretation of $Corr^2$(NDVI,P) as the fraction of the variance of NDVI "explained" by
335 variations in *P*. Equation (1) allows us to isolate this part of NDVI variability from that
336 associated with other sources, such as variations in radiation or nutrients as well as interference
337 from clouds, water vapor, and aerosols (Los et al. 2000).

338 A few notes are required regarding the estimation of Var(NDVI)*. First, by using the
339 annual totals for precipitation, we are assuming that a given year's precipitation represents the
340 water available that year for growth. Of course, other averaging periods for the precipitation
341 could have been employed (e.g., Zeng et al. 2013). The patterns in $Corr^2$(NDVI,P) obtained with
342 these other averaging periods, however, turn out to be the same, to first order; correlation maps
343 generated using 6-month or 9-month precipitation averages (not shown) are very similar to those
344 generated with the annual precipitation. Note that using the annual precipitation rather than the
345 contemporaneous 3-month precipitation has an important advantage: it reflects the fact that
346 antecedent precipitation can provide water to vegetation growth through storage in ground
347 reservoirs and snowpack (Milly, 1994).

348 Second, the observations are known to be subject to significant contamination from
349 clouds in high latitudes and from pollution in Southeast Asia (Fensholt and Proud, 2012), the
350 upshot being that small and artifactual negative correlations between NDVI and precipitation are
351 often seen in these regions. These negative correlations are problematic for our analysis. We
352 zero them out before computing $Corr^2$(NDVI,P), making the explicit assumption that any such
353 negative correlations represent noise. Note that even on the off chance that the negative
354 correlations are real, they would not represent the physical relationship we are after in this paper,
355 namely, the ability of water limitations to limit vegetation growth.

356 Figure 6a shows the distribution of Var(NDVI)*, as computed with (1). The patterns are
357 quite interesting: the regions for which moisture-related NDVI variability is high tend to
358 coincide with the Earth's grassland regimes – in the Great Plains of the U.S., the Nordeste region
359 of Brazil, the African Sahel, the Asian steppes, and eastern and northern Australia (see Figure 7).
360 The Var(NDVI)* patterns do miss grassland areas in India and China, but as shown in Figure 7,
361 these areas are subject to extensive irrigation (Siebert et al. 2005), a supply of water not
362 accounted for in the $Corr^2$(NDVI,P) diagnostic. Figure 6 demonstrates that, aside from such
363 irrigated areas, the locations of the Earth's grassland areas can be identified reasonably well from
364 the joint analysis of NDVI and precipitation data. The same patterns, and thus the same
365 connections to grassland regimes, are seen for Var(FPAR)*, the portion of the interannual
366 variance in 3-month FPAR averages related to moisture variations.

367 The results obtained with the dynamic phenology model are remarkably similar. A
368 comparison of Figures 6b and 6c shows that the model captures very well the observed spatial
369 pattern Var(FPAR)*, though again with a bias, as indicated by the different scaling factors used
370 for the plotting. Overall, the model successfully captures the role of hydroclimate in
371 determining the spatial distribution of interannual variability in phenology.

372

373 **4. Model Experiments**

374 Having demonstrated the Catchment-CN model's ability to capture the basic
375 hydroclimatic controls on phenology seen in the observations, we now use model experiments to
376 address key questions regarding the connections between hydroclimate and vegetation.

377

a. Influence of vegetation type on phenological variability

Clouding the interpretation of the Catchment-CN model's performance relative to observations in Section 3 above is the possibility that its use of prescribed vegetation types is somehow guaranteeing correct model behavior. Given, for example, that the observed distribution of Var(FPAR)* in Figure 6b captures well the locations of the world's grasslands (Figure 7), we must consider the possibility that high values of Var(FPAR)* are encouraged by the unique properties of grassland and discouraged by the properties of forests and shrubs, so that by imposing the observed vegetation distributions in the model, we artificially guarantee high simulated values of Var(FPAR)* in the correct areas (Figure 6c). The more intriguing possibility to consider, however, is that a specific hydroclimatic regime is responsible for high Var(FPAR)* values, a regime for which only grasslands happen to survive. With this second possibility, the vegetation type does not cause the Var(FPAR)* value; rather, the vegetation type and the Var(FPAR)* value are together controlled by something else, namely, the local moments of precipitation.

To examine this issue, we performed a repeat of the simulation described above, but with a twist: grassland vegetation was imposed on all land surfaces, and no other vegetation types were allowed to exist. Thus, in this experiment, vegetation type could not affect in any way the simulated spatial and temporal distributions of FPAR. Note that in this experiment, grassland is placed even in the driest deserts and in the wettest tropical areas; if the local climate is not conducive to grassland's survival, the grass is accordingly allowed to die out.

Figure 8c shows the spatial distribution of Var(FPAR)* for the all-grassland simulation. The plot captures, to first order, the features seen in the original model plot, supporting the

second possibility noted above. That is, the presence of grassland does not lead to high Var(FPAR)* values; the high values are instead indicative of a hydroclimatic regime that also happens to support grassland best. Similarly, the all-grassland simulation shows a relationship between FPAR maxima, mean precipitation, and precipitation variability (Figure 8a) that agrees to first order with that seen in the original model simulation (Figure 5f). The fact that FPAR tends to be highest in very wet conditions, for example, is not simply the result of the presence of dense forests in wet areas; the wet conditions themselves encourage the high FPAR values, and wet areas also tend to be where dense forests tend to flourish.

We repeated the simulation still again, this time after prescribing a deciduous forest vegetation type everywhere. The results, shown in Figures 8b and 8d, are essentially the same. Hydroclimatic variability, more than vegetation type, appears to dominate phenological variability – in the model and, we can infer, in nature.

b. Hydroclimate and the global carbon cycle

As noted in the introduction, a unique advantage of a model that can simulate phenology is its ability to provide information on additional, difficult to measure quantities. While carbon fluxes such as gross primary productivity (GPP), net primary productivity (NPP), and net ecosystem exchange (NEE) have been measured at various tower sites (Baldocchi 2008), directly observed global distributions of land-atmosphere carbon exchange are nonexistent. Model simulations, however, can readily provide these fields, and many examples of such simulated distributions already appear in the literature (e.g., Friedlingstein 2006). (We note that other

421 approaches for inferring global fields, such as machine learning algorithms that upscale from the
422 site measurements, are also available [Jung et al. 2011].)

423 Here we provide model-based estimates of the connection between carbon exchange and
424 hydroclimatic variability, focusing mainly on GPP. We first provide in Figure 9a this particular
425 model's vision of the global distribution of GPP. Because GPP is a flux rather than a
426 manifestation of vegetation state, we present it in terms of annual averages rather than for a 3-
427 month maximum period. The distributions have the expected maxima in the densely forested
428 tropics, with swaths of high values in the boreal forests of the north. Figures 9b and 9c show the
429 corresponding GPP fields from the simulations prescribing grassland and deciduous tree types,
430 respectively. The three panels show some differences but are, to first order, very similar,
431 indicating that vegetation type alone is not the main source of spatial variations in GPP; both
432 GPP and vegetation distributions are apparently controlled in tandem by something else.

433 Naturally, that "something else" is water availability. Figure 10 shows, in analogy to
434 Figure 4, the square of the spatial correlation between GPP and various meteorological forcing
435 variables. For all three simulations (control, "all grass", and "all trees"), precipitation mean and
436 variability have the dominant impact on GPP, with an r^2 of about 0.55 for the multiple regression
437 of GPP on $\log_{10}P$ and $\log_{10}\sigma_P$. Adding in the annual temperature and net radiation information
438 increases the r^2 to about 0.65. The fact that the r^2 values do not increase by much for the
439 uniform vegetation experiments suggests once again that variations in vegetation type do not by
440 themselves contribute significantly to spatial variations in GPP; the remaining unexplained
441 variance in Figure 10a presumably results from spatial variability in, for example, the seasonal
442 cycles and shorter-term temporal structure of the forcing quantities.

443 Figure 11 shows how precipitation means and variability control the spatial distribution
444 of GPP using scatter plots analogous to those shown in Figure 5. As with FPAR, GPP tends to
445 increase with increasing moisture availability (x-axis) and decreasing interannual variability (y-
446 axis), regardless of which vegetation types are assigned at the surface.

447 In contrast to Figure 5, Figure 11 uses a nonlinear scale for the shading, a scale that
448 shows the dominance of precipitation means over precipitation variability in determining GPP.
449 The impact of precipitation variability on GPP, however, is nevertheless significant. This is
450 demonstrated with a supplemental model simulation ("ClimP") in which we prescribed standard,
451 spatially varying vegetation types (as in the control simulation) but a modified precipitation
452 forcing: at each grid cell in ClimP, we scaled the precipitation forcing in each month of each year
453 so that the seasonal cycle of monthly totals for the year matched the long-term (climatological)
454 seasonal cycle. Thus, in ClimP, we artificially removed the monthly-scale year-to-year temporal
455 variability in the precipitation forcing – at each grid cell, the mean precipitation applied was
456 identical to that used in the control simulation, whereas the interannual variability of monthly
457 precipitation was, by construction, set to zero.

458 Figure 12 shows the difference between the mean annual GPP produced in ClimP and
459 that in the control simulation. Regions with large positive differences appear in the southeast
460 U.S., along the eastern coasts of South America and Australia, in the Indian subcontinent, in
461 northeastern China, and in various other regions of South America and Africa. Negative
462 differences do not appear anywhere. In effect, Figure 12 illustrates where GPP in the real world
463 would be larger if the year-to-year precipitation supply were more dependable – i.e., where the
464 interannual variability of precipitation holds down the land surface's carbon uptake. Note,
465 however, that human activities can mitigate the effects of this variability. India, southeast Asia,

and northeastern China in particular are known to undergo extensive irrigation (Figure 8). Because irrigation is effectively a means of providing a more dependable water supply, these particular areas may, in the real world, be capturing the larger GPP rates.

With Figure 13, we focus on the interannual variability of GPP at each grid cell rather than on the spatial distribution of its mean. Figure 13a shows the variance of annual GPP. Figure 13b shows the spatial distribution of $Corr^2(GPP,P)$, where P is the annual precipitation; that is, Figure 13b shows the fraction of the total GPP variance that is associated with, or can be "explained by", variations in annual water supply. The fractions are reasonably large across the globe, even in some areas considered to be not strongly water-stressed, such as the southeastern United States. In contrast, the fields of $Corr^2(GPP,T)$ and $Corr^2(GPP,R_{net})$, where T is the yearly-averaged temperature and R_{net} is the yearly-averaged net radiation, show significantly lower values (Figures 13c and 13d). While interannual temperature variations do have some impact on high latitude GPP variations (perhaps through their effects on snowcover duration), they have little impact anywhere else. Interannual net radiation variations appear to contribute more, especially in Africa; it is quite possible, however, that these particular "contributions" are not real and instead simply reflect known existing correlations between precipitation and net radiation there (not shown).

Together, annual precipitation, temperature, and net radiation do not explain all of the simulated GPP variability. As before, presumably a significant part of the variability stems from year-to-year variations in (for example) the sub-annual timing of the precipitation and associated variations in infiltration and runoff.

Figure 14 shows one final interesting result regarding the interannual variability of GPP. The shading shows Var(GPP) for a 3-month averaging period (centered, at each grid cell, around the month of maximum GPP). Overlain on the plot are black dots indicating where Var(FPAR) for 3-month averages (centered around the local monthly maximum for FPAR) exceeds a value of 0.003, an arbitrary threshold chosen for plotting convenience. The figure shows that Var(GPP) and Var(FPAR) tend not to be maximized in the same regions; Var(GPP) maxima tend to lie on the wetter sides of the Var(FPAR) maxima. The same basic result (not shown) is found for comparisons of the water-limited portions of the variances (i.e., Var(GPP)* versus Var(FPAR)*), and it is also found (not shown) for the all-grassland and all-deciduous-trees simulations, suggesting that variations in vegetation type are not responsible for such spatial offsets in the maxima. The spatial offsets are instead induced by the carbon physics built into the modeling system. Assuming these physical treatments are accurate, then similar offsets would apply to the real world's distributions of Var(GPP) and Var(FPAR). In other words, given estimates of Var(FPAR) attained, for example, through the processing of the GIMMS data, knowledge of the offsets could potentially help in the construction of an estimated spatial field of Var(GPP).

4. Summary and Discussion

Using the Catchment-CN model, a merger of the dynamic phenology components of the CLM4 dynamic vegetation model with the water and energy budget framework of the GMAO Catchment LSM, we examine the connections across the globe between hydroclimate and vegetation variables. Justification for the use of this model in such a study is provided by its demonstrated ability to reproduce observed connections between FPAR and precipitation moments (Section 3), namely, the increase in FPAR with increasing mean precipitation and

510 decreasing precipitation variability and the proper geographical placement of spatial maxima in
511 the global field of moisture-related FPAR variance.

512 Our model results can be summarized as follows. First, based on our supplemental
513 simulations with globally uniform vegetation type, we find that the aforementioned relationships
514 between FPAR and precipitation moments are largely independent of vegetation type; the fact
515 that trees grow in wet regimes, grass grows in drier regimes, and shrubs grow in even drier
516 regimes has only a second-order impact on the spatial distribution of FPAR and its interannual
517 variability at each location. Instead, hydroclimatic moments appear to be the dominant
518 determinants of both vegetation type and phenological expression, as represented by FPAR. Our
519 second basic result is that hydroclimatic moments provide a similarly dominant control over the
520 spatial and temporal variability of gross primary productivity (GPP), again with only a second-
521 order contribution from vegetation type.

522 Such a global scale description of GPP connections to hydroclimate is achievable with a
523 DVM but is not possible with observations, which are much more spatially and temporally
524 limited. Knapp and Smith (2001) used observations collected across eleven tower sites to show
525 that aboveground net primary production (ANPP) tends to increase with increasing annual
526 precipitation, and our global scale results (for GPP, a related variable) are consistent with this.
527 We do see some inconsistencies, however, with their study. For example, Knapp and Smith
528 (2001) find that ANPP has its maximum interannual variability in grassland areas. We find that
529 while the interannual variability of FPAR is maximized in grassland areas, the maxima for GPP
530 variability tend to be spatially offset from these FPAR variance maxima (Figure 14), slightly
531 toward the wetter (forested) side. The offset is minor, however, and the apparent inconsistency,
532 while certainly a possible result of model deficiencies, may also relate to the limited number of

tower sites they examined. More importantly, Knapp and Smith (2001) find that "interannual variability in ANPP [is] not related to variability in precipitation". Results from our control simulation (not shown) indicate that the square of the spatial correlation coefficient between Var(GPP) and Var(P) across land points is of the order of 30%, which disagrees with their conclusion; indeed, when we limit the calculation to values at the grid cells containing the LTER sites they studied, the square of correlation coefficient increases. We also find a reasonably strong relationship between the time series of GPP and precipitation (Figure 13b) at individual locations.

While interpretations of DVM-based results must be tempered by knowledge of model biases and limitations, DVM experiments, if properly interpreted, open the door to a wealth of potential studies of the global carbon cycle and its interactions with the global water and energy cycles. This paper provides one such study. Another example of note is provided by Guan et al. (2012), who show with DVM simulations over Africa that the statistical character of precipitation forcing (e.g., rainfall intensity) manifests itself in the GPP produced. The advantages of using DVMs – their provision of comprehensive (and often unmeasurable) data and their ability to be modified at will to allow the examination of the impacts of individual physical processes – stand them in good stead for future carbon analyses. Our understanding of global carbon-water-energy connections should continue to increase as researchers continue to use ever-improving versions of these tools.

555 **References**

556

557 Adler, R.F., G.J. Huffman, P.R. Keehn, 1994: Global tropical rain estimates from microwave-
558 adjusted geosynchronous IR data, Remote Sensing Rev., 11, 125-152.

559 Adler, R.F., G.J. Huffman, A. Chang, R. Ferraro, P. Xie, J. Janowiak, B. Rudolf, U. Schneider,
560 S. Curtis, D. Bolvin, A. Gruber, J. Susskind, and P. Arkin, 2003: The version 2 Global
561 Precipitation Climatology Project (GPCP) monthly precipitation analysis (1979-present),
562 *J. Hydrometeor.*, *4,* 1147-1167.

563 Baldocchi, D., 2008: 'Breathing' of the terrestrial biosphere: lessons learned from a global
564 network of carbon dioxide flux measurement system. Australian Journal of Botany, 56,
565 1-26.

566 Beck, H. E., T. R. McVicar, A. I. J. M. van Dijk, J. Schellekens, R. A. M. de Jeu, and L. A.
567 Bruijnzeel, 2011: Global evaluation of four AVHRR-NDVI data sets, Intercomparison
568 and assessment against Landsat imagery. Rem. Sen. Environ., 115, 2547-2563.

569 Berry, J. A., D. J. Beerling, and P. J. Franks, 2010: Stomata, Key players in the Earth system,
570 Past and present. Curr. Opinion in Plant Biol., 13, 233-240.

571 Boussetta, S., and Co-authors, 2012: Natural land carbon dioxide exchanges in the ECMWF
572 Integrated Forecasting System, Implementation and offline validation. ECMWF Tech.
573 Memo. 675, European Centre for Medium-Range Weather Forecasts, Shinfield Park,
574 Reading, Berkshire RG29AX, England.

575 Bowling, D. R., S. Bethers-Marchetti, C. K. Lunch, E. E. Grote, and J. Belnap, 2010: Carbon,
576 water, and energy fluxes in a semiarid cold desert grassland during and following
577 multiyear drought. J. Geophys. Res., 115, G04026, doi:10.1029/2010JG001322.

578 Budyko, M. I., 1974: *Climate and Life*. Academic Press, New York, 508 pp.

579 Choudhury, B., 1987: Relationships between vegetation indices, radiation, absorption, and net
580 photosynthesis evaluated by a sensitivity analysis. Remote Sens. Environ., 22, 209-233.

581 Dirmeyer, P. A., X. Gao, M. Zhao, Z. Guo, T. Oki, and N. Hanasaki, 2006: GSWP-2
582 Multimodel Analysis and Implications for Our Perception of the Land Surface, *Bul.*
583 *Amer. Meteo. Soc.*, **87**(10),1387-1397 DOI: 10.1175/BAMS-87-10-1381.

584 Dunne, J. P., and Co-authors, 2013: GFDL's ESM2 global coupled climate-carbon Earth system
585 models, Part 2, Carbon system formulation and baseline simulation characteristics. J.
586 Climate, 26, 2247-2252.

587 Fang, J., and Co-authors, 2005: Precipitation patterns alter growth of temperate vegetation.
588 Geophys. Res. Lett., 32, L21411, doi:10.1029/2005GL024231.

589 Fensholt, R., and S. R. Proud, 2012: Evaluation of Earth Observation based global long term
590 vegetation trends – Comparing GIMMS and MODIS global NDVI time series. Remote
591 Sens. Environ., 119, 131-147.

592 Friedlingstein, P., and Co-authors, 2006: Climate–carbon cycle feedback analysis, Results from
593 the C4MIP model intercomparison. J. Climate, 19, 3337-3353.

Goward, S. N., and K. F. Huemmrich, 1992: Vegetation canopy PAR absorbance and the normalized difference vegetation index, An assessment using the SAIL model. Remote Sens. Environ., 39, 119-140.

Guan, K., E. F. Wood, D. Medvigy, K. K. Caylor, S. S. Good, and J. Sheffield, 2012: Quantify the impacts of seasonal variability in precipitation on vegetation functions in Africa. Poster presented at AGU Fall Meeting, San Francisco, CA, December 2012.

Hall, F. G., and Co-authors, 2006: ISLSCP Initiative II global data sets, Surface boundary conditions and atmospheric forcings for land-atmosphere studies. J. Geophys. Res., 11, D22S01, doi:10.1029/2006JD007366.

Ichii, K., A. Kawabata, and Y. Yamaguchi, 2002: Global correlation analysis for NDVI and climatic variables and NDVI trends, 1982-1990. Int. J. Rem. Sens, 23, 3873-3878.

Jahan, N., and T. Y. Gan, 2011: Modelling the vegetation-climate relationship in a boreal mixedwood forest of Alberta using normalized difference and enhanced vegetation indices. Int. J. Rem. Sens., 32, 313-335.

Jung, M., and Co-authors, 2011: Global patterns of land-atmosphere fluxes of carbon dioxide, latent heat, and sensible heat derived from eddy covariance, satellite, and meteorological observations. J. Geophys. Res., 116, G00J07, doi:10.1029/2010JG001566.

Kaufman, Y. J., D. d. Herring, K. J. Ranson, and G. J. Collatz, 1998: Earth Observing System AM1 mission to Earth. IEEE Trans. Geosci. Rem. Sens., 36, 1045-1055.

Knapp, A. K., and M. D. Smith, 2001: Variation among biomes in temporal dynamics of aboveground primary production. Science, 291, 481-484.

615 Koster, R. D., M. J. Suarez, A. Ducharne, M. Stieglitz, and P. Kumar, 2000: A catchment-based
616 approach to modeling land surface processes in a general circulation model: 1. Model
617 structure, *J. Geophys. Res.*, **105**(20), 24,809– 24,822.

618 Krinner, G., and Co-authors, 2005: A dynamic global vegetation model for studies of the coupled
619 atmosphere-biosphere system. Global Biogeochem. Cycles, 19, GB1015,
620 doi:10.1029/2003GB002199.

621 Lawrence, D. M., K. W. Oleson, M. G. Flanner, P. E. Thornton, S. S. Swenson, P. J. Lawrence,
622 X. Zeng, L. Yang, S. Levis, K. Sakaguchi, G. B. Bonan and A. G. Slater, 2010:
623 Parameterization improvements and functional and structural advances in version 4 of the
624 Community Land Model. Journal of Advances in Modeling Earth Systems, 3: doi:
625 10.1029/2011MS000045 DOI: doi: 10.1029/2011MS000045.

626 Leuning, R., and Co-authors, 2004: Spatial and temporal variations in fluxes of energy, water
627 vapour, and carbon dioxide during OASIS 1994 and 1995. Boundary Layer Meteorol.,
628 110, 3-38.

629 Los, S. O., G. J. Collatz, P. J. Sellers, C. M. Malmstrom, N. H. Pollack, R. S. DeFries, L.
630 Bounoua, M. T. Parris, C. J. Tucker, and D. A. Dazlich, 2000: A global 9-yr biophysical
631 land surface dataset from NOAA AVHRR data, Journal of Hydrometeorology, 1, 183-
632 199.

633 Milly, P. C. D., 1994: Climate, soil water storage, and the average annual water balance. *Water*
634 *Resour. Res.*, **30**, 2143-2156.

635 Moore, I. D., P. E. Gessler, G. A. Nielsen, and G. A. Petersen, 1993: Terrain attributes,
636 estimation methods and scale effects. In: Modeling Change in Environmental Systems,
637 edited by A. J. Jakeman, M. B. Beck, and M. McAleer, Wiley, London, 189-214.

638 Oleson, K. W., and Co-authors, 2010: Technical description of version 4.0 of the Community
639 Land Model (CLM). NCAR Technical Note NCAR/TN-478+STR., National Center for
640 Atmospheric Research, P. O. Box 3000, Boulder, Colorado, 80307-3000.

641 Puma, M. J., R. D. Koster, and B. I. Cook, 2013: Phenological versus meteorological controls on
642 land-atmosphere water and carbon fluxes. J. Geophys. Res., 118,
643 doi:10.1029/2012JG002088.

644 Sellers, P. J., S. O. Los, C. J. Tucker, C. O. Justice, D. A. Dazlich, G. J. Collatz, and D. A.
645 Randall, 1996: A revised land surface parameterization (SiB2) for atmospheric GCMs,
646 Part II, The generation of global fields of terrestrial biophysical parameters from satellite
647 data. J. Climate, 9, 706-737.

648 Sellers, P. J., and Co-authors, 1997: Modeling the exchanges of energy, water, and carbon
649 between continents and the atmosphere. Science, 275, 502-509.

650 Sheffield, J., G. Goteti, and E. F. Wood, 2006: Development of a 50-year high-resolution global
651 dataset of meteorological forcings for land surface modeling. *J. Climate*, *19*, 3088-3111.

652 Siebert, S. , P. Doll, J. Hoogeveen, J. M. Faures, K. Frenken, and S. Feick, 2005: Development
653 and validation of the global map of irrigation areas. Hydrol. and Earth Syst. Sci., 9, 535-
654 547.

655 Thornton, P. E., S. C. Doney, K. Lindsay, J. K. Moore, N. Mahowald, J. T. Randerson, I. Fung,
656 J. F. Lamarque, J. J. Feddema and Y. H. Lee, 2009: Carbon-nitrogen interactions regulate
657 climate-carbon cycle feedbacks: results from an atmosphere-ocean general circulation
658 model. Biogeosciences, 6(10), 2099-2120

659 Trenberth, K. E., J. T. Fasullo, and J. Mackaro, 2011: Atmospheric moisture transports from
660 ocean to land and global energy flows in reanalyses. J. Climate, 24, 4907-4924.

661 Tucker, C. J., and Co-authors, 2005: An extended AVHRR 8-km NDVI dataset compatible with
662 MODIS and SPOT vegetation NDVI data. Int. J. Rem. Sens., 26, 4485-4498.

663 Wang, G. and E. A. B. Eltahir, 2000: Biosphere-atmosphere interactions over West Africa, 2,
664 Multiple climate equilibria. Q. J. R. Meteorol. Soc., 126, 1261-1280.

665 Zeng, N., J. D. Neelin, K.-M. Lau, and C. J. Tucker, 1999: Enhancement of interdecadal climate
666 variability in the Sahel by vegetation interaction. Science, 286, 1537-1540.

667 Zeng, F.-W., G. J. Collatz, J. E. Pinzon, and A. Ivanoff, 2013: Analysis of the relationship
668 between climate and NDVI variability at global scales. Manuscript submitted to Remote
669 Sensing.

670

671 **List of Figures**

672 Figure 1. a. Schematic of flux computations in the original Catchment LSM. b. Schematic of
673 flux computations in the merged model, Catchment-CN.

674 Figure 2. Schematic of independent vegetation (carbon) treatments in topographically-defined
675 vegetation zones. Three static vegetation zones are defined, with independent carbon
676 prognostic variables in each. W_1, W_2, and W_3 are soil moisture states in the three
677 dynamically-varying hydrological zones (with time-varying areas AR1, AR2, and AR3);
678 weighted averages of these states (e.g, W_{V2}, as shown in the figure) and corresponding
679 weighed temperature states are passed down to the carbon physics calculations for the
680 different vegetation zones.

681 Figure 3. a. Distribution of average NDVI in peak NDVI season (the month for which the mean
682 seasonal cycle of NDVI is maximized along with the preceding and following months),
683 from GIMMS observations. The peak season varies with grid cell; see text for details. b.
684 Same, but for average FPAR in peak FPAR season, from GIMMS observations. c. Same,
685 but for average FPAR in peak FPAR season, from model simulation.

686 Figure 4. (a) Square of the spatial correlation coefficient (over land grid cells) between observed
687 NDVI and land surface forcing variables: the logarithm of the mean annual precipitation
688 (P), the logarithm of the standard deviation of annual precipitation (σ_P), mean annual air
689 temperature (T), and mean annual net radiation (R_{net}). The final two bars show the square
690 of the correlation coefficient obtained from the multiple regression of NDVI against,
691 respectively, (i) precipitation mean and standard deviation, and (ii) all four quantities. (b)
692 Same, but for observed FPAR. (c) Same, but for modeled FPAR.

693 Figure 5. (a) Average GIMMS NDVI in peak NDVI season as a function of the mean
694 precipitation (x-coordinate) and the standard deviation of annual precipitation (y-
695 coordinate). Each dot represents a single land grid cell. (b) Same as (a), but with the
696 individual values in the scatter plot averaged over bins. At least 5 dots must lie within a
697 bin for the binned value to be plotted. (c) and (d): Same as (a) and (b), but for GIMSS
698 FPAR data. (e) and (f): Same as (a) and (b) , but for model-simulated FPAR data.

699 Figure 6. (a) Product of the interannual variance of GIMMS NDVI data averaged over the
700 maximum NDVI season and the square of the correlation between NDVI and annual
701 precipitation, multiplied by 1000. (b) Same, but for GIMMS FPAR data. (c) Same, but
702 for model-generated FPAR data, and with the scaling factor changed to 500.

703 Figure 7. Map of grassland locations, as derived from the distributions used in the Second Phase
704 of the Global Soil Wetness Project (Dirmeyer et al. 2006). The dots overlain on the plot
705 indicate regions for which irrigation is extensive (>10% of the land area, based on data
706 aggregated from FAO [http://www.fao.org/nr/water/aquastat/irrigationmap/index.stm]),
707 suggesting difficulty in relating observations-based FPAR values to local precipitation
708 amounts.

709 Figure 8. (a) Same as Figure 2f (average model-simulated FPAR in peak FPAR season as a
710 function of the mean precipitation and the standard deviation of annual precipitation), but
711 for the case in which the entire globe is forced to be covered by grassland. (b) Same as
712 (a), but for the “all tree” case. (c) Same as Figure 6c (product of the interannual variance
713 of model-simulated FPAR averaged over the maximum FPAR season and the square of
714 the correlation between NDVI and annual precipitation, multiplied by 500), but for case

where the entire globe is forced to be covered by grassland. (d) Same as (c), but for the "all tree" case.

Figure 9. Global distribution of annual gross primary productivity (GPP, in grams C / m^2-day) for: (a) the control simulation; (b) the simulation in which all land is covered with a grassland vegetation type; and (c) the simulation in which all land is covered with a deciduous tree vegetation type.

Figure 10. (a) Same as Figure 4, but for GPP (rather than NDVI or FPAR) produced in the control simulation. (b) Same, but for GPP produced in the "all grass" simulation. (c) Same, but for GPP produced in the "all trees" simulation.

Figure 11. (a) Average GPP (g Carbon / m^2-day) as a function of the mean precipitation (x-coordinate) and the standard deviation of annual precipitation (y-coordinate) in the control simulation, with individual land grid cell values averaged over bins. At least 5 dots must lie within a bin for the binned value to be plotted. (b) Same, but for the simulation in which all land is covered with a grassland vegetation type. (c) Same, but for the simulation in which all land is covered with a deciduous tree vegetation type.

Figure 12. Difference in the mean annual GPP produced in the ClimP simulation (the simulation using climatological precipitation forcing) and that produced in the control simulation, in units of grams carbon/m^2-day.

Figure 13. (a) Variance of annual GPP (in g^2 / m^4day^2) as produced by the control simulation. (b) $Corr^2$(GPP,P), i.e., the fraction of the GPP variance associated with interannual variance in annual precipitation. (c) Same as (b), but for the fraction of the GPP

736 variance associated with interannual variations in annual temperature. (d) Same as (b),
737 but for the fraction of the GPP variance associated with variations in annual net radiation.

738 Figure 14. Interannual variance of GPP (g^2/m^4day^2) for the 3-month period centered on the
739 month for which the local GPP is climatologically largest. Overlain on the plot are black
740 dots showing where the interannual variance of 3-month FPAR is maximized.

741

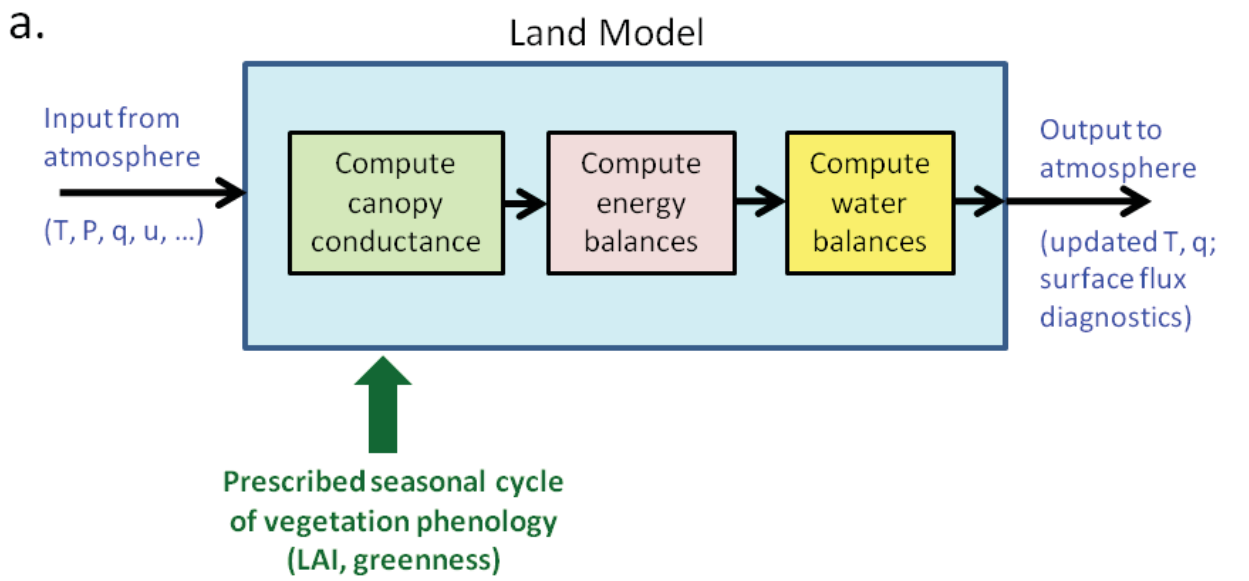

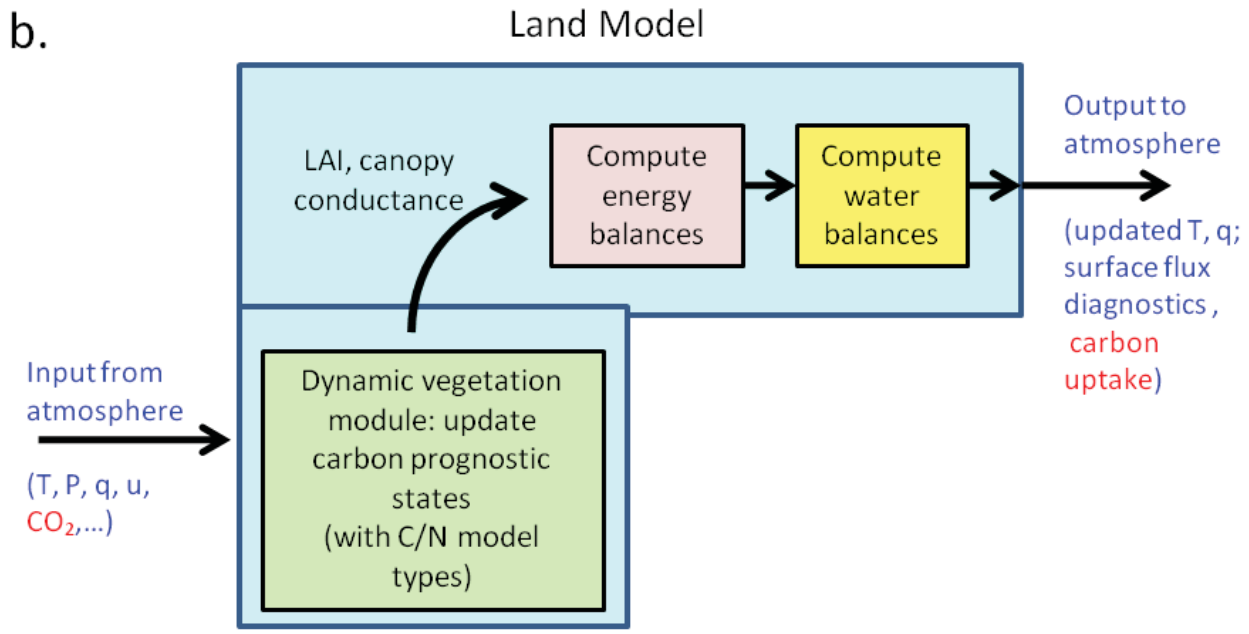

Figure 1. a. Schematic of flux computations in the original Catchment LSM. b. Schematic of flux computations in the merged model, Catchment-CN.

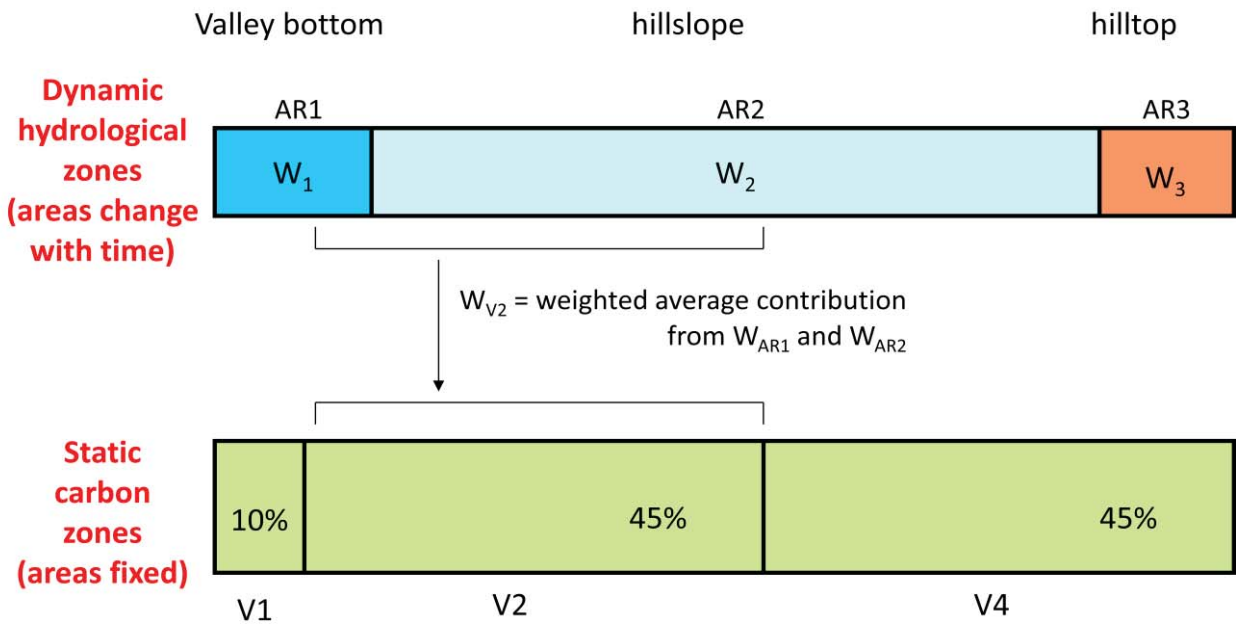

Figure 2. Schematic of independent vegetation (carbon) treatments in topographically-defined vegetation zones. Three static vegetation zones are defined, with independent carbon prognostic variables in each. W_1, W_2, and W_3 are soil moisture states in the three dynamically-varying hydrological zones (with time-varying areas AR1, AR2, and AR3); weighted averages of these states (e.g, W_{V2}, as shown in the figure) and corresponding weighed temperature states are passed down to the carbon physics calculations for the different vegetation zones. Weighted averages of vegetation zone quantities (e.g., canopy conductance) are similarly passed back to the hydrological zones.

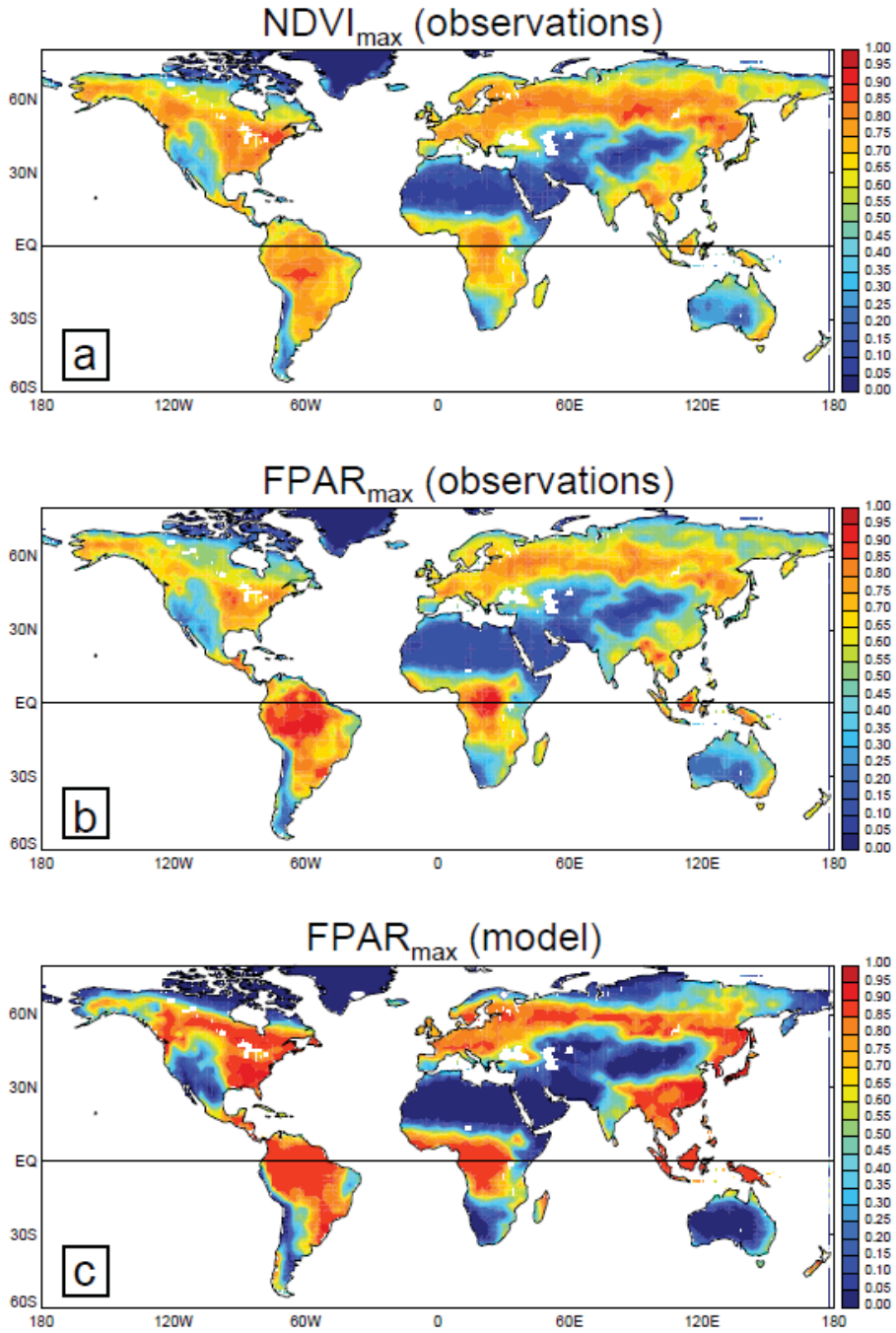

Figure 3. a. Distribution of average NDVI in peak NDVI season (the month for which the mean seasonal cycle of NDVI is maximized along with the preceding and following months), from GIMMS observations. The peak season varies with grid cell; see text for details. b. Same, but for average FPAR in peak FPAR season, from GIMMS observations. c. Same, but for average FPAR in peak FPAR season, from model simulation.

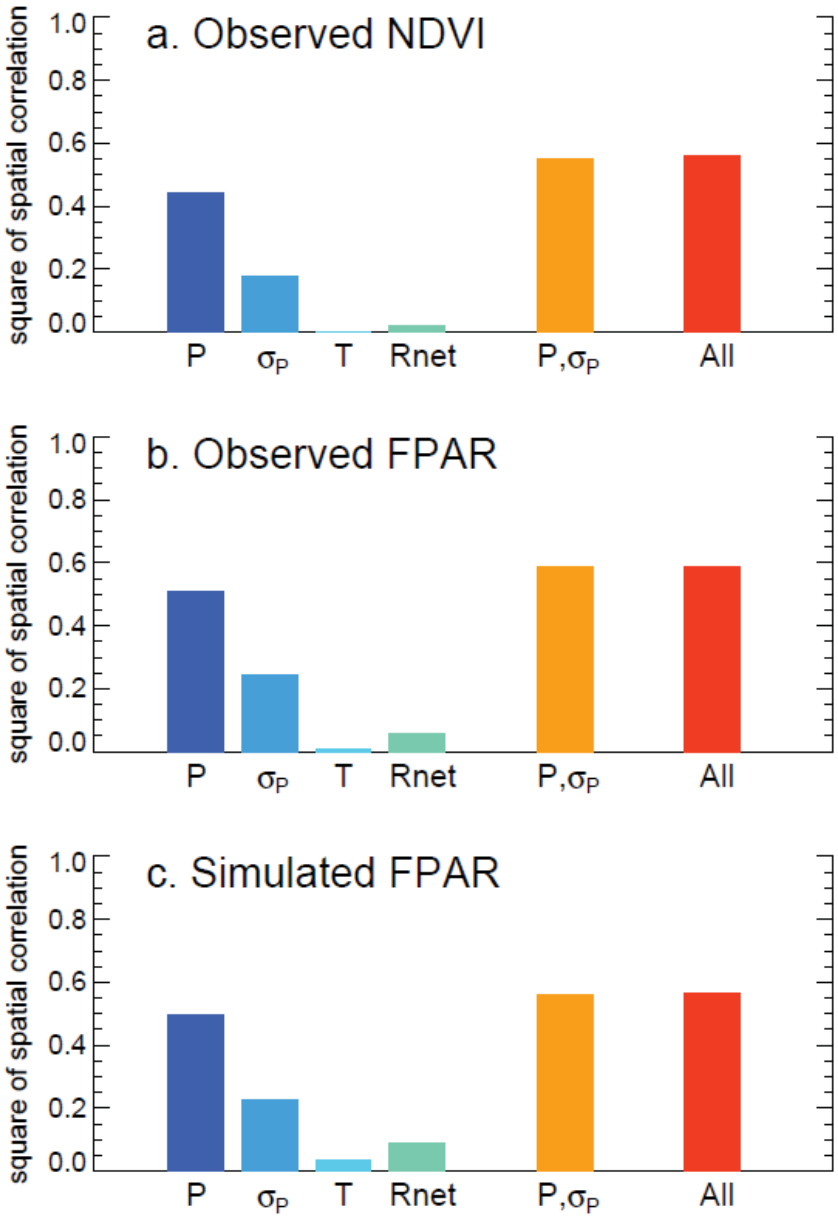

Figure 4. (a) Square of the spatial correlation coefficient (over land grid cells) between observed NDVI and land surface forcing variables: the logarithm of the mean annual precipitation (P), the logarithm of the standard deviation of annual precipitation (σ_P), mean annual air temperature (T), and mean annual net radiation (R_{net}). The final two bars show the square of the correlation coefficient obtained from the multiple regression of NDVI against, respectively, (i) precipitation mean and standard deviation, and (ii) all four quantities. (b) Same, but for observed FPAR. (c) Same, but for modeled FPAR.

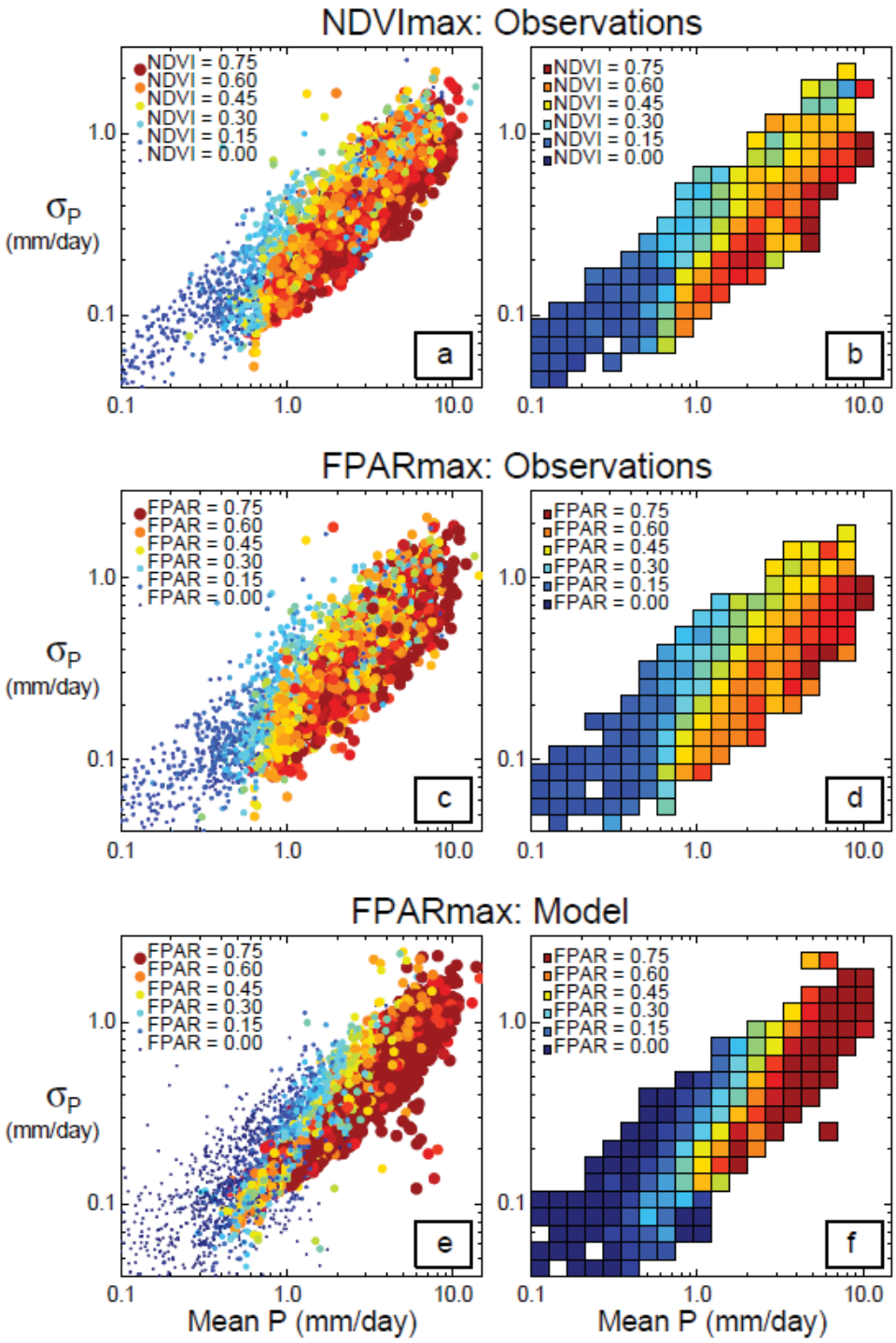

Figure 5. (a) Average GIMMS NDVI in peak NDVI season as a function of the mean precipitation (x-coordinate) and the standard deviation of annual precipitation (y-coordinate). Each dot represents a single land grid cell. (b) Same as (a), but with the individual values in the scatter plot averaged over bins. At least 5 dots must lie within a bin for the binned value to be plotted. (c) and (d): Same as (a) and (b), but for GIMSS FPAR data. (e) and (f): Same as (a) and (b) , but for model-simulated FPAR data.

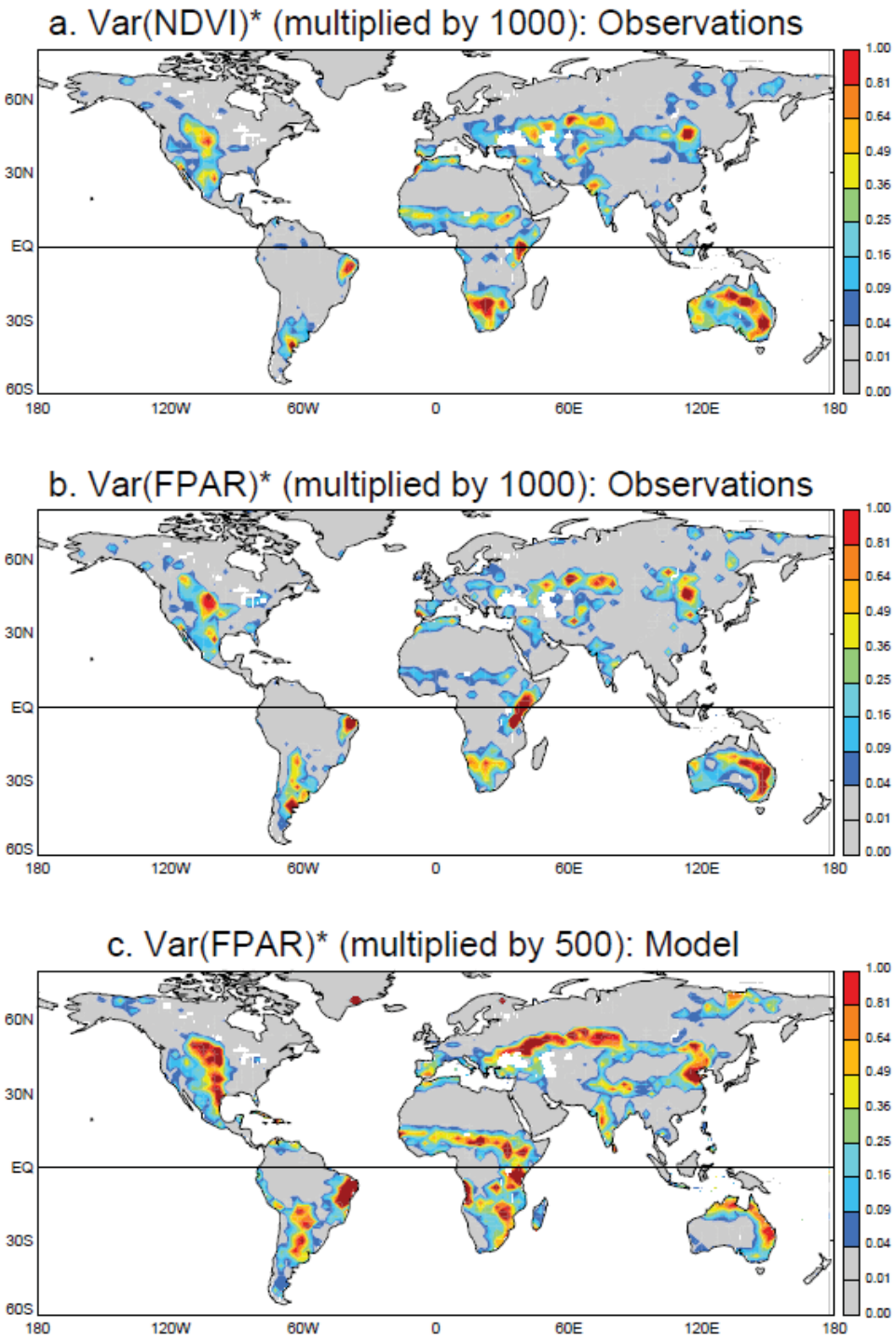

785

786 Figure 6. (a) Product of the interannual variance of GIMMS NDVI data averaged over the
787 maximum NDVI season and the square of the correlation between NDVI and annual
788 precipitation, multiplied by 1000. (b) Same, but for GIMMS FPAR data. (c) Same, but for
789 model-generated FPAR data, and with the scaling factor changed to 500.

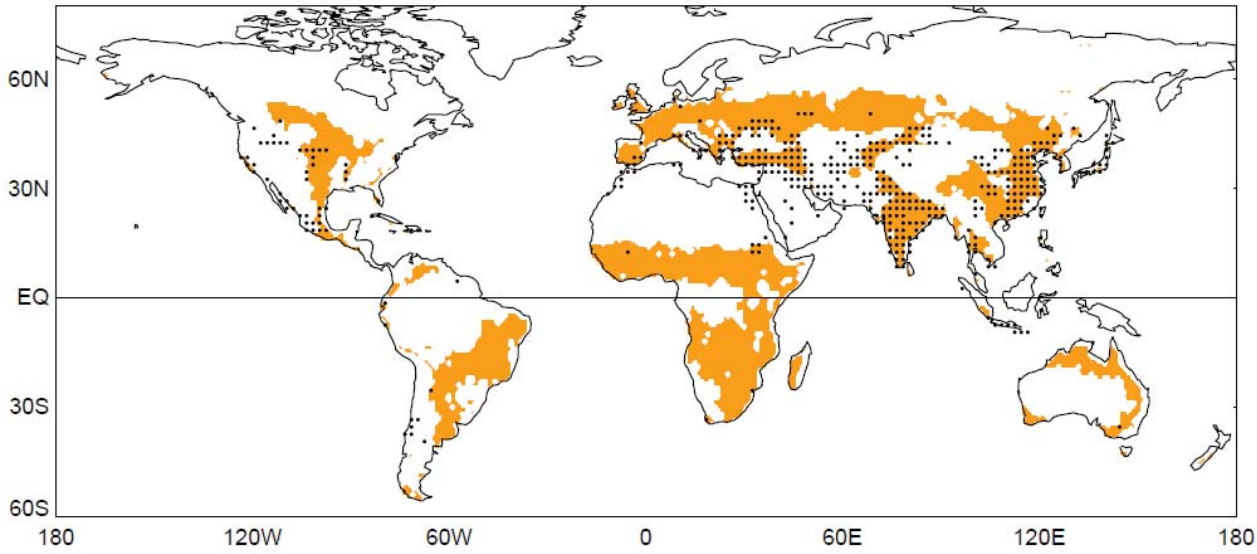

790

791

792 Figure 7. Map of grassland locations, as derived from the distributions used in the Second Phase
793 of the Global Soil Wetness Project (Dirmeyer et al. 2006). The dots overlain on the plot indicate
794 regions for which irrigation is extensive (>10% of the land area, based on data aggregated from
795 FAO [http://www.fao.org/nr/water/aquastat/irrigationmap/index.stm]), suggesting difficulty in
796 relating observations-based FPAR values to local precipitation amounts.

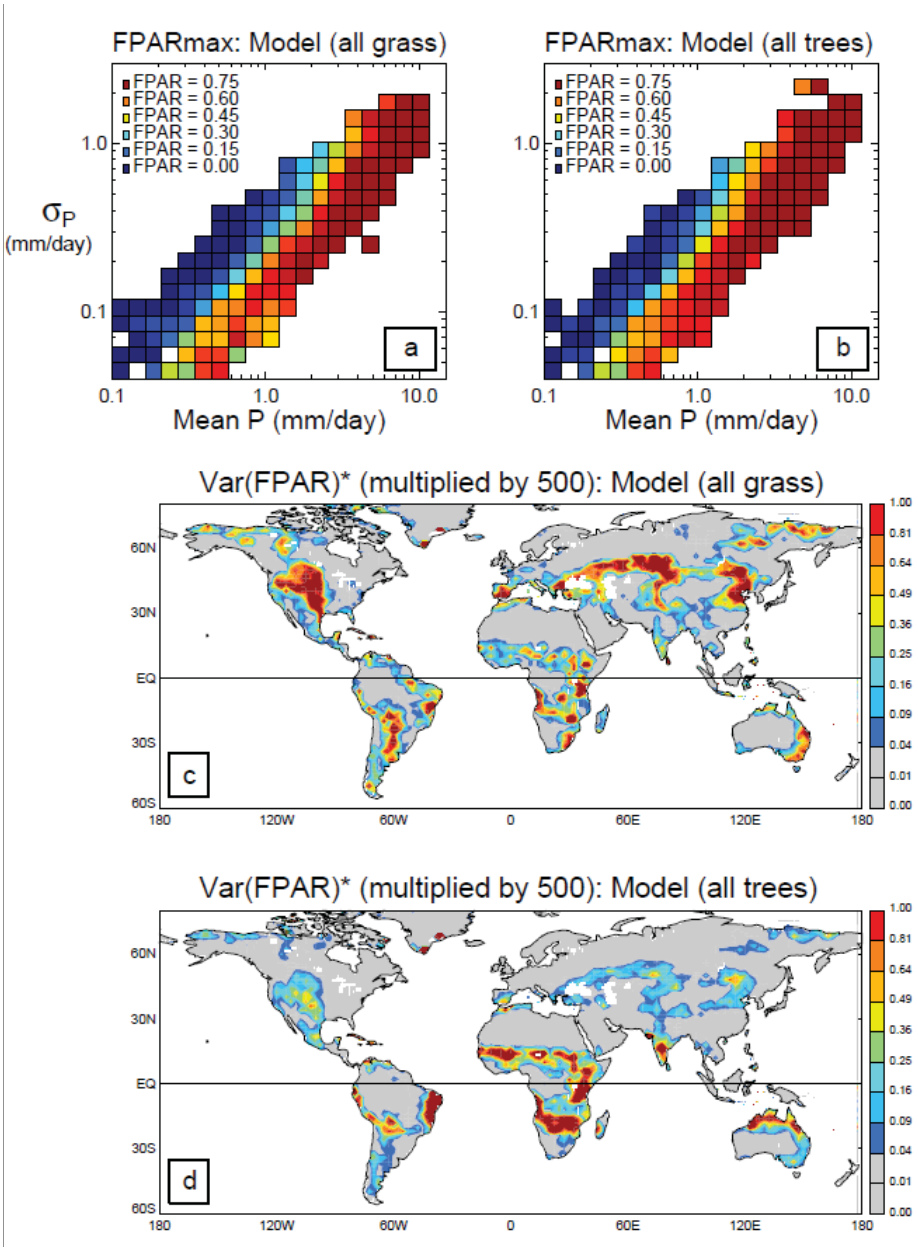

Figure 8. (a) Same as Figure 2f (average model-simulated FPAR in peak FPAR season as a function of the mean precipitation and the standard deviation of annual precipitation), but for the case in which the entire globe is forced to be covered by grassland. (b) Same as (a), but for the "all tree" case. (c) Same as Figure 6c (product of the interannual variance of model-simulated FPAR averaged over the maximum FPAR season and the square of the correlation between NDVI and annual precipitation, multiplied by 500), but for case where the entire globe is forced to be covered by grassland. (d) Same as (c), but for the "all tree" case.

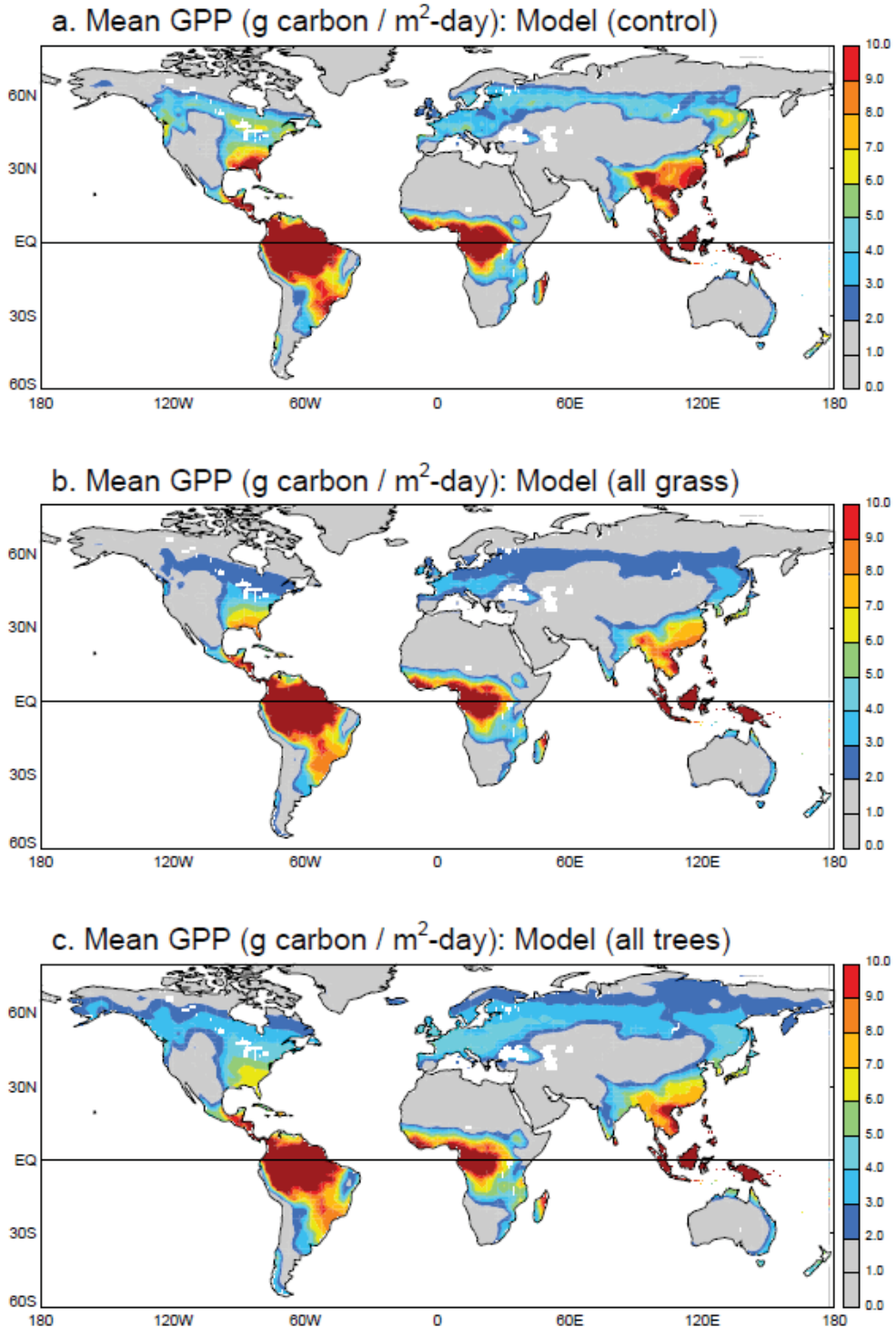

807

808 Figure 9. Global distribution of annual gross primary productivity (GPP, in grams C / m^2-day)
809 for: (a) the control simulation; (b) the simulation in which all land is covered with a grassland
810 vegetation type; and (c) the simulation in which all land is covered with a deciduous tree
811 vegetation type.

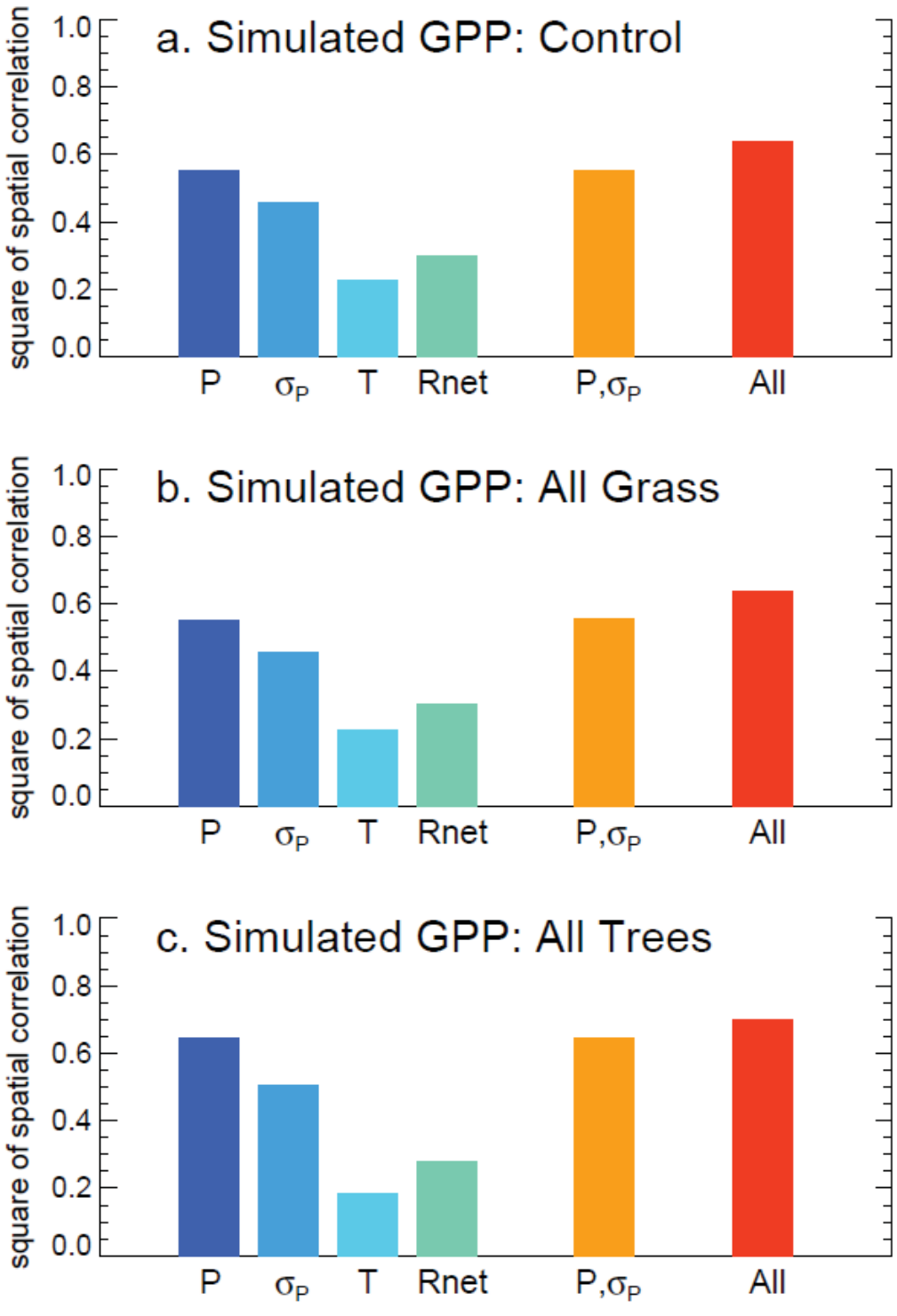

Figure 10. (a) Same as Figure 4, but for GPP (rather than NDVI or FPAR) produced in the control simulation. (b) Same, but for GPP produced in the "all grass" simulation. (c) Same, but for GPP produced in the "all trees" simulation.

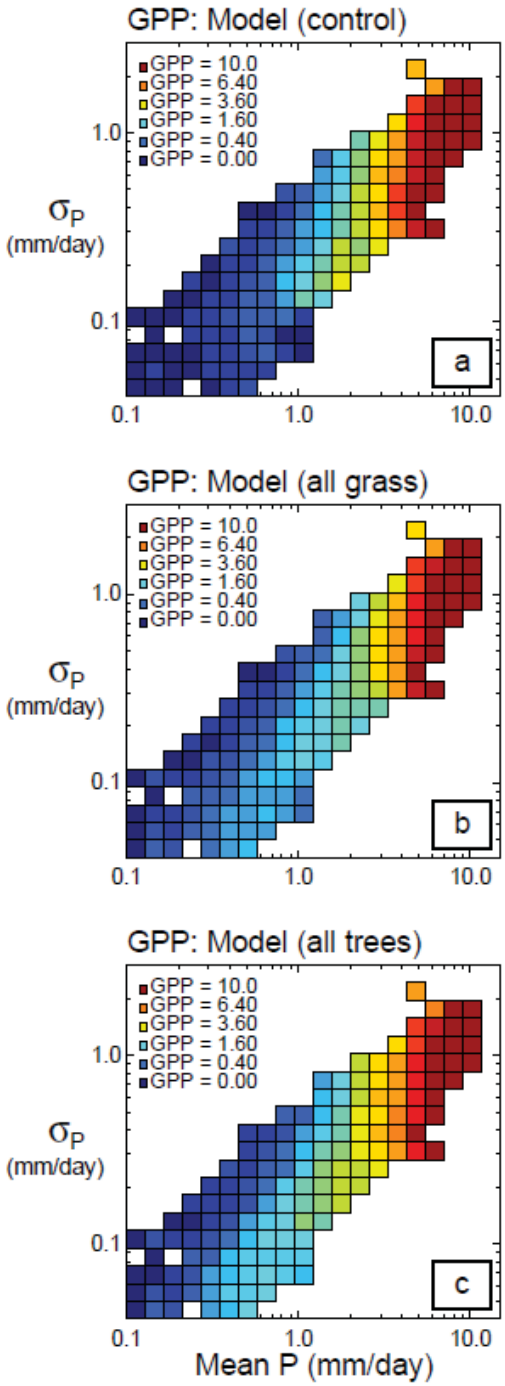

817

818 Figure 11. (a) Average GPP (g Carbon / m^2-day) as a function of the mean precipitation (x-
819 coordinate) and the standard deviation of annual precipitation (y-coordinate) in the control
820 simulation, with individual land grid cell values averaged over bins. At least 5 dots must lie
821 within a bin for the binned value to be plotted. (b) Same, but for the simulation in which all land
822 is covered with a grassland vegetation type. (c) Same, but for the simulation in which all land is
823 covered with a deciduous tree vegetation type.

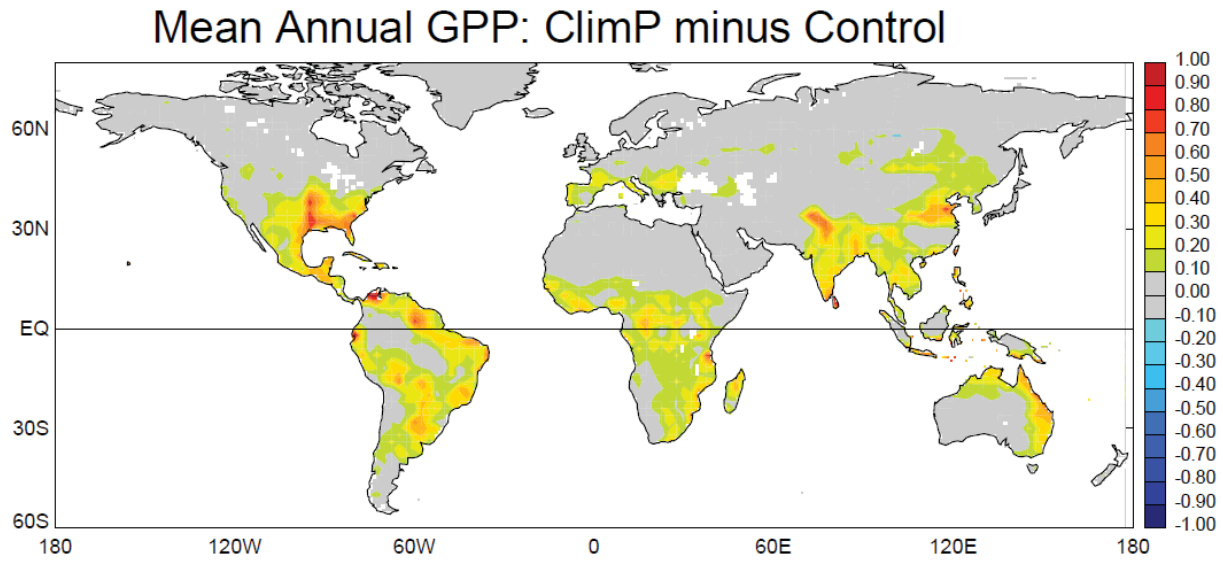

Figure 12. Difference in the mean annual GPP produced in the ClimP simulation (the simulation using climatological precipitation forcing) and that produced in the control simulation, in units of grams carbon/m^2-day.

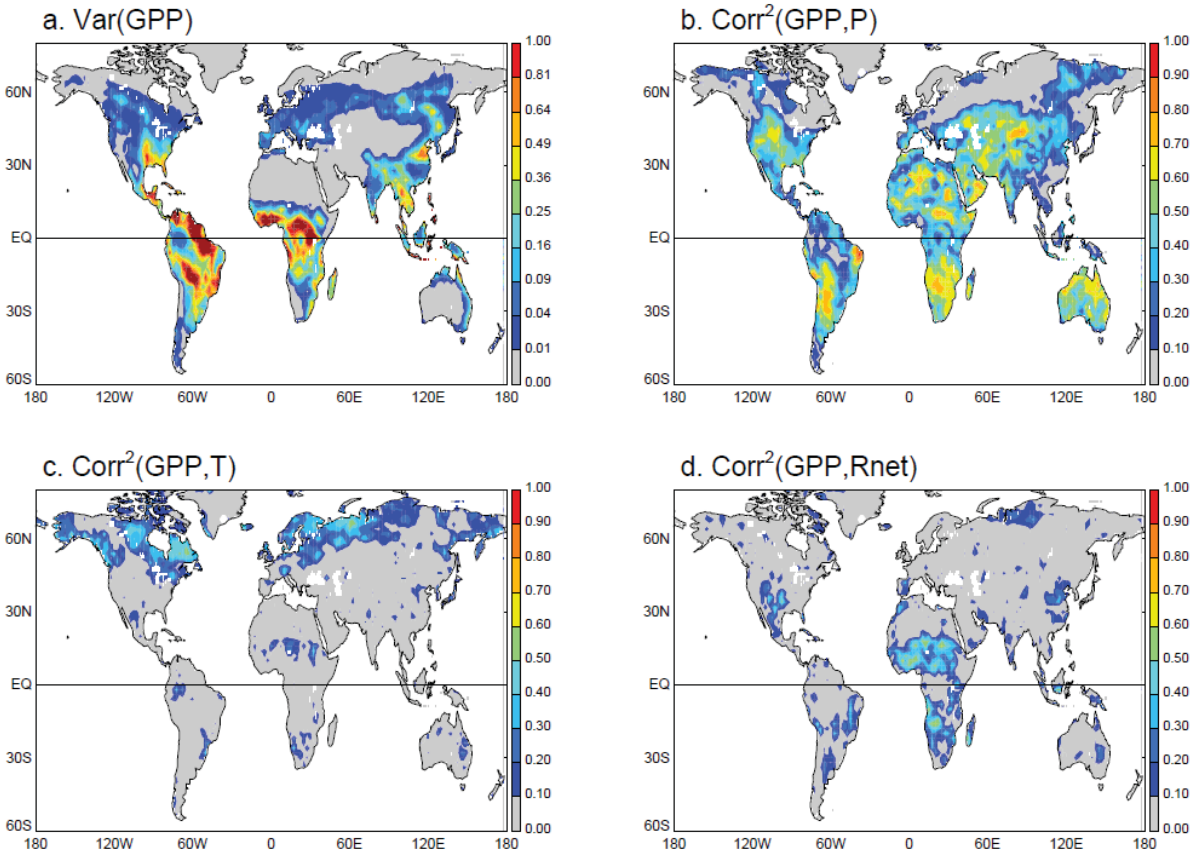

833

834

835 Figure 13. (a) Variance of annual GPP (in g^2 / $m^4 day^2$) as produced by the control simulation.
836 (b) $Corr^2$(GPP,P), i.e., the fraction of the GPP variance associated with interannual variance in
837 annual precipitation. (c) Same as (b), but for the fraction of the GPP variance associated with
838 interannual variations in annual temperature. (d) Same as (b), but for the fraction of the GPP
839 variance associated with variations in annual net radiation.

840

841

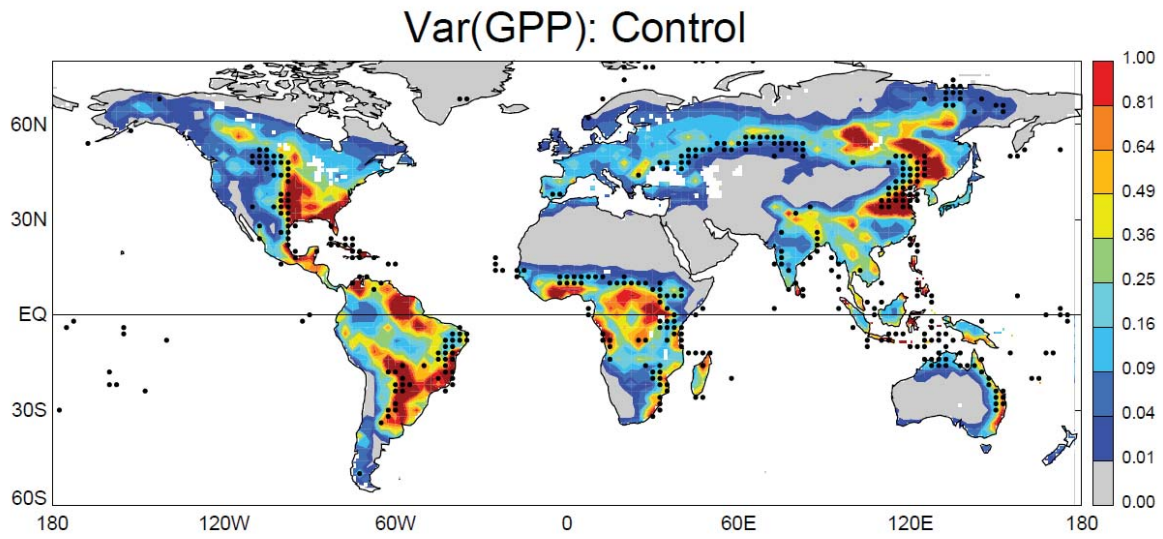

842

843

844 Figure 14. Interannual variance of GPP (g^2/m^4day^2) for the 3-month period centered on the
845 month for which the local GPP is climatologically largest. Overlain on the plot are black dots
846 showing where the interannual variance of 3-month FPAR is maximized.